

Automatic reconstruction of the arterial and venous trees on volumetric chest CT

Seyoun Park, Sang Min Lee, Namkug Kim,^{a)} and Joon Beom Seo

Department of Radiology, University of Ulsan College of Medicine, Asan Medical Center, Seoul 138-736, South Korea

Hayong Shin

Department of Industrial and Systems Engineering, Korea Advanced Institute of Science and Technology, Daejeon 305-701, South Korea

(Received 24 February 2013; revised 24 May 2013; accepted for publication 28 May 2013; published 24 June 2013)

Purpose: This paper introduces a novel approach to classify pulmonary arteries and veins from volumetric chest computed tomography (CT) images. Although there is known to be a relationship between the alteration of vessel distributions and the progress of various pulmonary diseases, there has been relatively little research on the quantification of pulmonary vessels *in vivo* due to morphological difficulties. In particular, there have been few efforts to quantify the morphology and distribution of only arteries or veins through automated algorithms despite the clinical importance of such work. In this study, the authors classify different types of vessels by constructing a tree structure from vascular points while minimizing the construction cost using the vascular geometries and features of CT images.

Methods: First, a vascular point set is extracted from an input volume and the weights of the points are calculated using the intensity, distance from the boundaries, and the Laplacian of the distance field. The tree construction cost is then defined as the summation of edge connection costs depending on the vertex weights. As a solution, the authors can obtain a minimum spanning tree whose branches correspond to different vessels. By cutting the edges in the mediastinal region, branches can be separated. From the root points of each branch, the cut region is regrouped toward the entries of pulmonary vessels in the same framework of the initial tree construction. After merging branches with the same orientation as much as possible, it can be determined manually whether a given vessel is an artery or vein. Our approach can handle with noncontrast CT images as well as vascular contrast enhanced images.

Results: For the validation, mathematical virtual phantoms and ten chronic obstructive pulmonary disease (COPD) noncontrast volumetric chest CT scans with submillimeter thickness were used. Based on experimental findings, the suggested approach shows 9.18 ± 0.33 (mean \pm SD) visual scores for ten datasets, 91% and 98% quantitative accuracies for two cases, a result which is clinically acceptable in terms of classification capability.

Conclusions: This automatic classification approach with minimal user interactions may be useful in assessing many pulmonary disease, such as pulmonary hypertension, interstitial lung disease and COPD. © 2013 American Association of Physicists in Medicine. [<http://dx.doi.org/10.1118/1.4811203>]

Key words: pulmonary artery and vein classification, pulmonary vessel segmentation, tree reconstruction

I. INTRODUCTION

Thanks to rapid progress of medical imaging techniques, we can now observe detailed anatomy *in vivo* at submillimeter spatial resolutions and use the observations as an aid for diagnoses. This has instigated a trend toward making radiology a more quantitative science.¹ However, there still remain many difficulties to quantify via automated algorithms. One of the unsolved problems is the pulmonary vascular segmentation and classification of arteries and veins on medical images.

Recently, several studies suggested that vascular alteration is closely related to endothelial dysfunction² which is claimed to be related to emphysema.^{3,4} From this point of view,

Matsuoka and co-workers^{5,6} recently attempted to show a correlation between the area of small pulmonary vessels and pulmonary function tests (PFT). To find small vessels, they select circular regions whose areas were less than 5 mm^2 after simple thresholding in a 2D computed tomography (CT) slice. Although this approach is simple and inaccurate from a technical viewpoint, their results nevertheless showed a strong clinical correlation between vessel distribution and PFT. In addition, there has been little research on the quantification of pulmonary vessels *in vivo*. In particular, there has almost no work devoted to distinguishing between arteries or veins in automated algorithms despite the clinical importance of doing so. For example, it is well known of expansion of

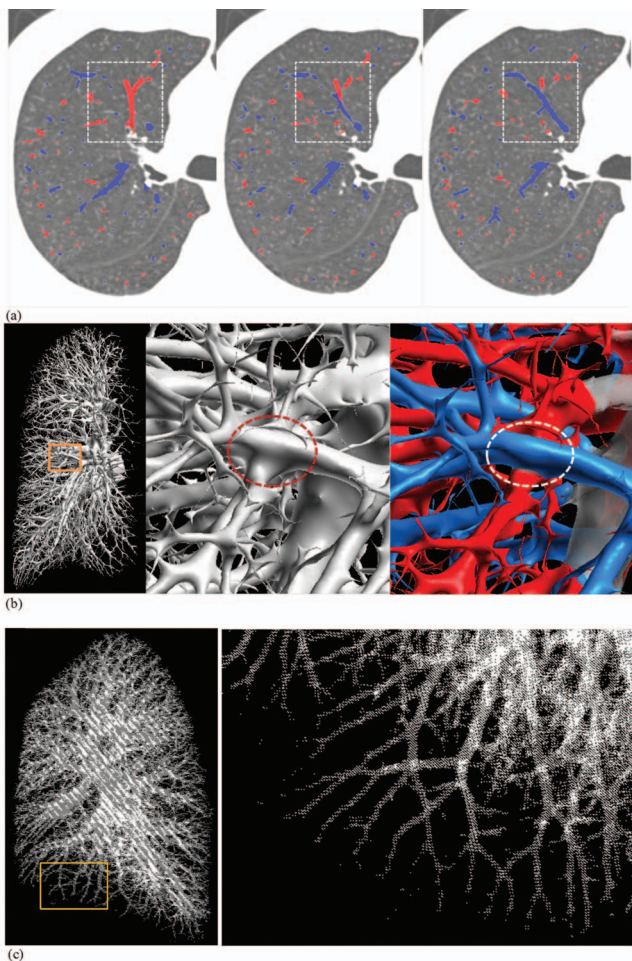


FIG. 1. Difficult cases of the automatic classification. (a) Consecutive slices of the crossing region in a right lung (foot-to-head). (b) 3D view of the crossing region in (a); the middle and the right figures are an enlarged region of the orange box in the left one. The circles in the figures show a closely crossing case. (c) Unevenly and sparsely distributed points.

pulmonary artery with pulmonary hypertension. However, little is known about the phenomenon in small arteries. From this point of view, we started this study to see the alterations of small vessels according to the types of vessels affected by different causes or locations of pulmonary disease. As the first step of this analysis, segmentation and classification of arteries and veins are necessary.

To accurately quantify the properties of pulmonary vessels, it is important to segment, classify, and analyze the target vessels with whole volumetric CT which is one of the best ways to analyze pulmonary structures *in vivo*.

However, an analysis of pulmonary arteries from medical images is not a trivial task due to the complicated vascular morphological structure as well as the limitations of current imaging technologies such as partial volume effects or other artifacts. In particular, it is difficult to automate the extraction of accurate vascular structures from noncontrast CT images. Furthermore, the creation of an explicit classification scheme for arteries and veins has not been successful, even if segmentation can be performed well.

Pulmonary vessels are distributed densely throughout the lung with different scales of size and attenuation intensities, as they branch and split into smaller structures. Their morphological properties, such as the radii and branching patterns, vary from person to person. Moreover, some arteries and veins pass closely, often crossing each other, and then some parts appear to be combined into a single region in the CT images. In contrast, there may be disconnected vascular trees as a result of disease, motion artifacts, or the partial volume effects of peripheral small vessels. Figure 1 shows an example of such a case.

To resolve these difficulties, we introduce a novel approach which classifies arteries and veins from volumetric chest CT images. Our method can handle noncontrast images as well as vascular contrast enhanced CT images. When starting this research, we were technically motivated by the tree reconstruction algorithm with 3D scanned point clouds. Considering the similarities between natural construction and branching patterns,⁷ we attempt to apply previous tree reconstruction approaches for point clouds to the construction of pulmonary vessel structure. The main difference is that it is important to maintain accurate depiction of the anatomical structure, and the classification of two different types of branches is necessary in the latter case. We analyze CT image data and transform our problem to optimization problem of construction cost for the vascular trees generation.

The main goal of this study is to develop an algorithm that separates and classifies arteries and veins automatically. The technical aims are as follows:

- To handle noncontrast volumetric CT images;
- To extract pulmonary vessels automatically;
- To classify different types of vessels automatically;
- To generate an efficient structure for a quantitative analysis;

Figure 2 shows a classification example of our approach to achieve these goals with the data shown in Fig. 1. This

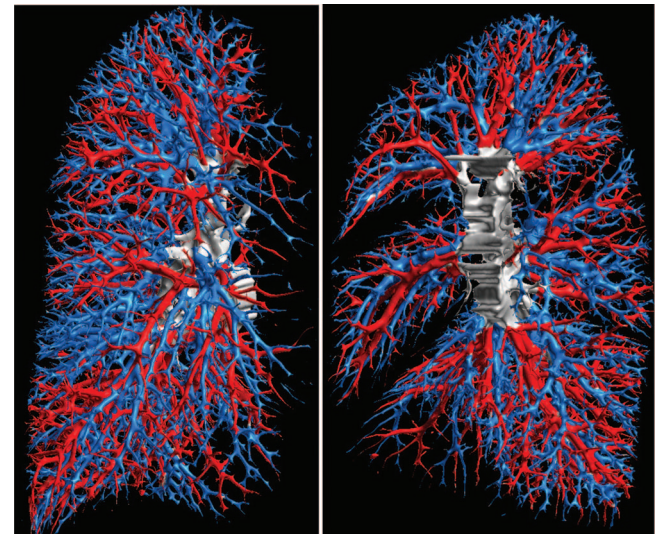


FIG. 2. The final result of pulmonary vessel segmentation and classification with the data in Fig. 1; 3D renderings at coronal view direction (left) and sagittal view direction (right).

result shows 9.2 acceptance level with visual scores by a human expert and 98% classification capability with quantified evaluation. The details are presented in Secs. II–VI. In Sec. II, previous related works are introduced, and the algorithms are described in detail from Secs. III–V. Finally, the validity of our approach is shown experimentally in Sec. VI.

II. RELATED WORK

Although a massive body of work has been devoted to extracting vessels (not specifically pulmonary vessels), the automatic or semiautomatic classification of pulmonary arteries from veins has not been extensively examined or performed successfully with chest CT images.

A typical means of vessel extraction in general organs with medical images involves the use of multiscale filters, which primarily are employed with magnetic resonance angiography (MRA) images.^{8,9} This approach applies Gaussian filters iteratively at different scales and analyzes local shapes with the eigenvalues of a Hessian matrix. Another approach is to use deformable models whose boundary surfaces are deformed from initial surfaces in a way that optimizes the given energy functions.¹⁰ The level set is also a widely used approach in vessel segmentation;^{11,12} it is simple when used to extract vessel structures with vascular contrast-enhanced images.

Specific to pulmonary vessels, simple thresholding and front-propagation techniques were initially explored by several groups.^{9,13–16} Level sets were also used by several groups,^{17,18} and Kaftan *et al.*¹⁹ introduced fuzzy theory to this problem. Agam *et al.*²⁰ introduced the fuzzy theory to vascular tree construction problem. Tozaki *et al.*²¹ tried to segment all types of pulmonary organs using CT images. From a different perspective, Chen *et al.*²² attempted to classify nodules from pulmonary vessels automatically with CT images.

There have also been several attempts to segment arteries explicitly from vessel segmentation results.^{19,23–25} However, those studies used contrast enhanced images or omitted thorough evaluations. One notable study was introduced by Saha *et al.*,²⁴ who computed a fuzzy distance transform and separate arteries and veins (A/V) by morphological opening from given seed points, later revising the result with user interactions.²⁶ Their study focused on how to separate combined vessels and did not explicitly deal with disconnected cases. Therefore, we suggest a more systematic way to treat vascular structure with high fidelity in this study.

Meanwhile, the tree reconstruction problem has been considered in many areas such as urban modeling in the computer graphics field. Livny's work,²⁷ the technical inspiration of this study, reconstructed multiple trees from unorganized point clouds, and Tan *et al.*²⁸ also modeled trees from images.

These techniques may be applied to our method through a combination with point set reconstruction approaches. One approach described in Ref. 29 reconstructed surfaces by extracting curve skeletons from a point cloud including large holes while another³⁰ reconstructed surfaces successfully from noisy and unorganized point clouds by introducing the concept of arterial snakes. Hassouna introduced a curve skeleton construction algorithm using a gradient vector flow, which

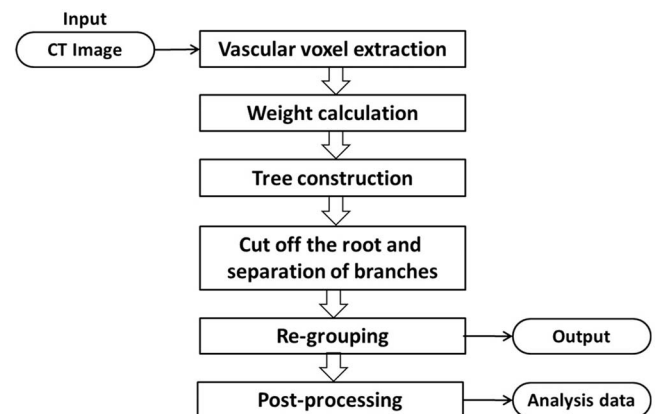


FIG. 3. Overall procedure of our approach.

is similar to our tree construction approach.³¹ However, they only focused on the skeleton construction of shapes. Moreover, their approach differs from that presented here in that our case includes other problems, such as crossing vessels.

Because the voxels in vessels can be treated as a point set, we combined these approaches with our vascular tree construction and classification problem, the overall procedure of which is shown in Fig. 3.

III. VESSEL DETECTION AND SEGMENTATION

As the preprocessing step of the classification process, we need to extract the voxels of vessel candidates from the CT images. This is performed via the following procedure. First, we identify closed regions of the lungs, which are generally represented as two separate segments in the volume data.¹⁴ This is a trivial task because the lungs show an accurate boundary with adjacent tissues or organs in CT images except for patients with severe lung disease. Here, we define simple volume geometries for the further steps.

The volumetric data have ranges that are expressed as $\mathbf{L} = (L_x, L_y, L_z)^T$ along each direction from a base corner point, an origin. The volume is composed of uniform grid cells, generally known as a *voxel*, which may be anisotropic; that is, the unit length of each cell may be represented independently as $\mathbf{d} = (d_x, d_y, d_z)^T$. The number of cells on each axis is expressed as $\mathbf{n} = (n_x, n_y, n_z)^T$. Let $\Gamma = \{\mathbf{c} \mid \mathbf{c} = (i, j, k), i = 1, \dots, n_x, j = 1, \dots, n_y, k = 1, \dots, n_z\}$ be the set of voxels constructed from CT scans and $I(\mathbf{c})$ be the attenuation intensity of a voxel \mathbf{c} . The lung segmentation results are stored in the set of voxels for the right lung, $L_R \subset \Gamma$, and the left lung $L_L \subset \Gamma$.

Before exploring the algorithmic details, we first examine the anatomical structure of the pulmonary vessels, using *a priori* knowledge based on this basic geometrical representation.

III.A. Pulmonary vessel anatomy

Figure 4 shows a simplified diagram of the right and left lungs from the mediastinal view. Typically, the bronchial

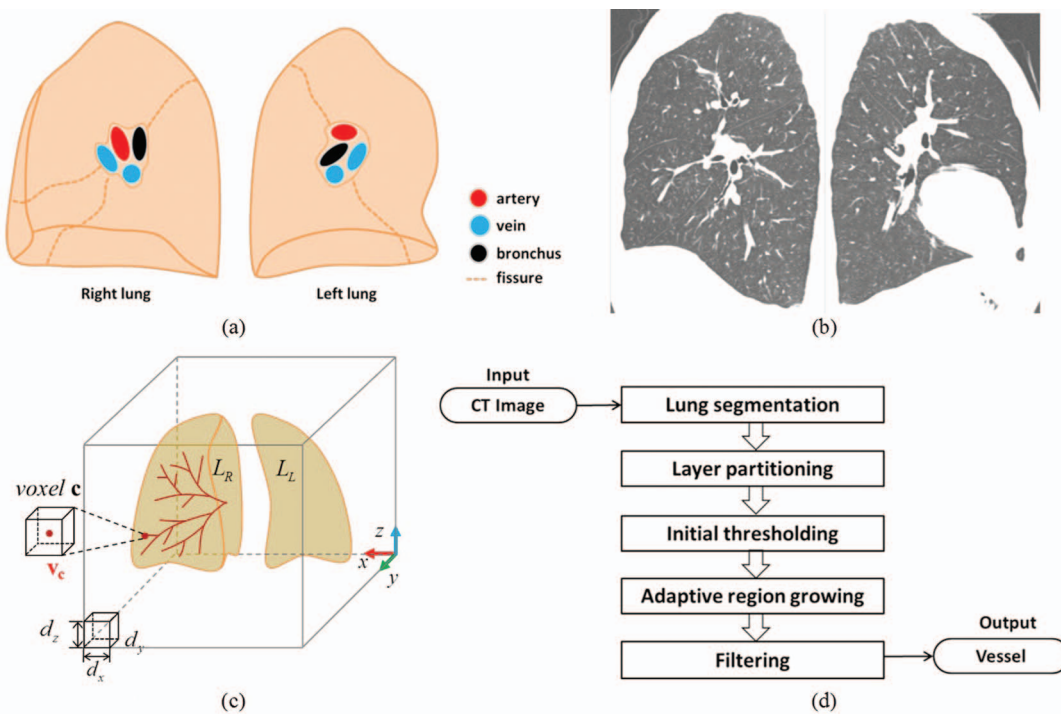


FIG. 4. Pulmonary vessel anatomies and segmentation procedure. (a) Schematic diagrams. (b) Corresponding CT images (sagittal view). (c) Volume geometries. (d) Vessel segmentation procedure.

branches and the pulmonary artery and two veins are located in the sectional view. As shown in Fig. 4, the entries of the artery and veins appear as if they attached to each other in the mediastinal region, as only the attenuation density is shown in grayscale intensities in the CT images. The bronchial walls and pulmonary vessels are often located closely to each other, and fissure lines have similar attenuation intensities to small vessels in noncontrast CT images.

III.B. Pulmonary vessel extraction

To apply our classification method, which is described in Secs. IV–V, it is necessary to extract vessels explicitly as a 3D point set. It is a very challenging issue to segment pulmonary vessels precisely.³² Because this step is not the main focus of this study, we apply an efficient approach with proper fidelity. Even though any successive approach may be used for this step, we need to approach this aspect carefully, as the vessel extraction result may affect to the classification result, especially when nonvascular structures are also selected.

For computational efficiency, we choose initial thresholding plus adaptive region growing rather than level sets or approaches based on an active-contour. First, we partition L_R and L_L into four layers each from the proximal to distal regions and extract voxels with different threshold ranges.³³ We then apply adaptive region growing³⁴ with a neighbor size of $5 \times 5 \times 5$.

Let the segmentation result $V = \{w(c)\}$ and let a set of vascular points $w(c) = (x, y, z, \mu)^T = (\mathbf{v}_c^T, \mu_c)^T$, where $\mathbf{v}_c = (x, y, z)^T = ((\mathbf{c}_i - 0.5) \times d_x, (\mathbf{c}_j - 0.5) \times d_y, (\mathbf{c}_k - 0.5) \times d_z)^T$ is the center position of voxel c , and $\mu = I(c)$ is the attenuation coefficient of c , which is expressed as the Hounsfield unit.

III.C. Filtering

Because we collect points using only intensities, nonvascular structures, such as small airway walls, fissures, and nodules, may be contained in the extraction result in the non-contrast image. As fissures may affect the classification result sensitively, we filter them via a tensor analysis using a Hessian matrix of I , where I is the intensity field of the volume. If the input image is vascular contrast-enhanced, this step may be skipped because vascular voxel intensities are represented in the higher range than other structures in a lung. Therefore, there is less chance of selecting nonvascular structures incorrectly during the segmentation process compared to noncontrast CT scans.

As is well known, all the voxels can be classified to one of the three local shape categories, a sphere (or a point), cylinder (or a line), or plane, by comparing the eigenvalue of the Hessian matrix $H(I)$.^{33,35} A sphere is a point in a thick (large) vessel, a cylinder is a point in a thin (small) vessel, and these are normal vessel points. A point in the plane (or surface) is likely to be on a fissure, meaning that we should remove them after classifying all of the points in V .

Another challenging task is extracting the wall of small airways or nodules precisely; this is, however, beyond the scope of this research. Also, our classification approach shows quite robust results in these two cases experimentally unless the nodule is much larger than the vessels. Figure 5 shows the vessel extraction results after removing the planar points from noncontrast chest CT images.

After obtaining the vessel points V , the main goal of the remaining work is to construct a connected structure of the points and to separate and group different branches of vessels.

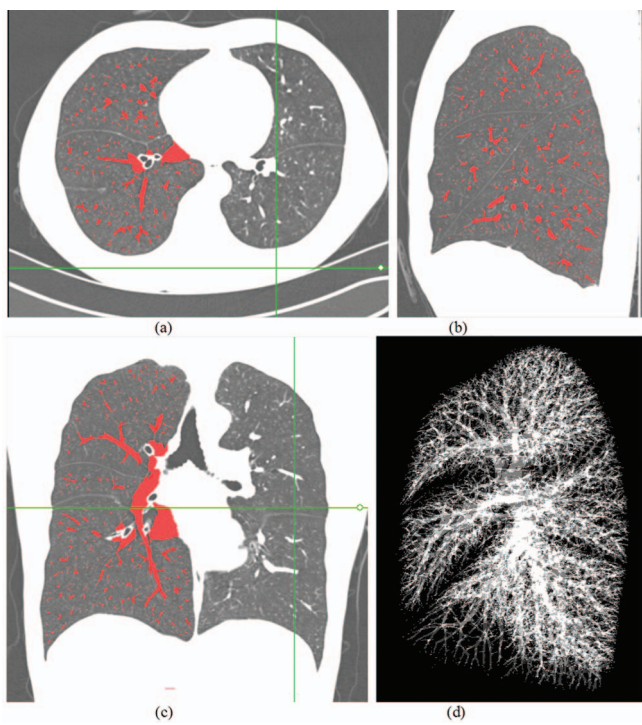


FIG. 5. Vessel segmentation results. (a) Axial view. (b) Sagittal view. (c) Coronal view. (d) Point set in 3D.

For this purpose, we create a tree data structure to connect the same branches of vessels. We can then easily refine the tree and estimate its properties.

IV. TREE CONSTRUCTION

One of the main contributions of this study is that it constructs a global tree structure whose branches correspond to the vascular structure for use in both classification and analysis. To do this, we define the tree construction energy first and compute an optimal structure.

IV.A. Initial tree construction

The problem in this study is to obtain the tree structure $T = (V, E)$ connecting all the vertices in V and whose construction energy (or cost) is the minimum of Eq. (1).

$$\min_T C(T). \quad (1)$$

Because the set of vertices V is already given in this case, the construction energy is only affected by the connections of edges; $C(T)$ is then defined as the summation of the connecting energy of edges, as in Eq. (2),

$$C(T) = \sum_{(i,j) \in E} C(i, j), \quad (2)$$

The construction energy of each edge connecting the i th and j th vertices is defined as Eq. (3),

$$C(i, j) = \frac{\|\mathbf{v}_j - \mathbf{v}_i\|}{\alpha + \beta w_j + \gamma e_{ij}}, \quad (3)$$

where $i, j \in \{1, \dots, |V|\}$ are the indexes of the vertices, \mathbf{v}_i and \mathbf{v}_j are the vertex position vectors, w_j is the weight of vertex j , and e_{ij} is the weight of the edge direction (i, j) depending on a local orientation vector of vertex j . $\alpha, \beta, \gamma (> 0)$ are positive real-value constants defined by users to be chosen appropriately; specifically, α serves to make the denominator $\neq 0$. We set $\alpha = 1/5$, $\beta = 3/5$, $\gamma = 1/5$ for the purpose of this study. The detailed meaning of each term is described in Secs. IV.A.1–IV.A.3. Our problem becomes determining the set of edges that minimizes the construction energy and connects all of the vertices. The solution naturally becomes therefore a minimum spanning tree (MST) whose generation algorithms are well-known.

IV.A.1. Weights of vertices

The weight of a vertex provides the connection priority or the degree of its ease of classification. If a point can be simply classified into one category, we should collect such points first. This is defined by the three factors of the attenuation density, the distance from the boundaries, and the Laplacian of the distance field. As attempted in previous works,^{13,36} we can connect centerlines to obtain a skeleton as a simplified structure of vessels. However, when moving more towards proximal or distal regions, it becomes progressively more difficult to extract an accurate centerline with only the distance field.

The weight of the i th vertex w_i ($i = 1, \dots, |V|$) is the average of three types of different weights such that $w_i = (w_i^1 + w_i^2 + w_i^3)/3$. $w^1 \in [0, 1]$ is the normalized intensity, which is defined as $w_i^1 = (\mu_i - \mu_{\min}) / (\mu_{\max} - \mu_{\min})$, where $\mu_{\max} = \max\{\mu_i\}$ and $\mu_{\min} = \min\{\mu_i\}$. As shown in Fig. 6, the attenuation intensity does not reflect the shape of the vessels unerringly and the blood does not flow along the centerline.³⁷ Therefore, we introduce $w^2 \in [0, 1]$ which is a normalized distance from the vessel boundaries. The normalized unsigned distance field from extracted vessel boundaries is denoted as Φ . We define the third weight as Eq. (4) using the characteristic that the Laplacian becomes $\nabla^2 \Phi \rightarrow +\infty$, where two isocontours collapse.

$$w^3 = \min\{1, 1 - s(\nabla^2 \Phi)\}. \quad (4)$$

Here, the function $s(x): \mathbf{R} \rightarrow \mathbf{R}$ makes the Laplacian scaled to $[-\tau, 1]$ ($\tau > 0$) such that the maximum value becomes 1. This is used to find the region that is “sandwiched” by two vessels.

Figure 6 shows each color-coded weight in sectional views and Fig. 7 shows the rendering of the final result after assigning intensities according to the weights. The centerlines of the vessels look brighter and the points close to the vessel walls appear darker.

IV.A.2. Cost of edges

After weights are assigned for vertices, we can then define the edge construction energy such that it becomes smaller when connecting spatially closer vertices with greater weights. To represent this, we assign the edge cost $C(i, j)$ by dividing the Euclidean distance between two vertices,

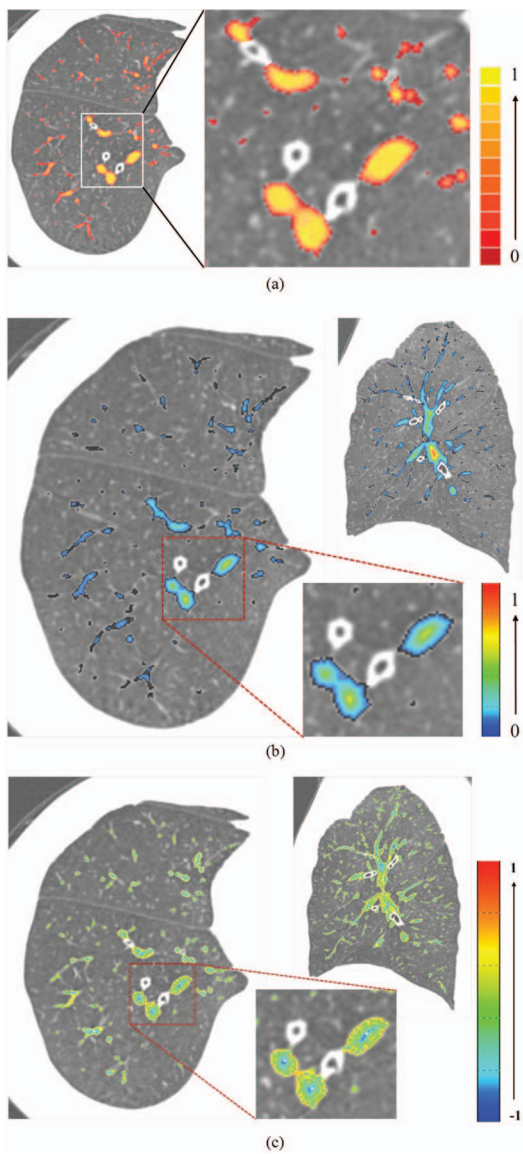


FIG. 6. Three vertex weight factors; 2D sectional views of the same position; the weight values of voxels are mapped to corresponding colors shown in the right side of each figure. (a) Normalized intensity of the vessels. (b) Normalized distance field from vessel boundary. (c) Scaled Laplacian of (b).

$\|\mathbf{v}_j - \mathbf{v}_i\|$, with the weight of the connected vertex w_j . One more aspect to be considered is the difference between the direction of the edge and the direction in which the vessels proceed. For this purpose, we define e_{ij} in Eq. (3) as Eq. (5).

$$e_{ij} = \begin{cases} 1, & \text{if } \mathbf{e}_j = \mathbf{0} \\ \left| \frac{(\mathbf{v}_j - \mathbf{v}_i)}{\|\mathbf{v}_j - \mathbf{v}_i\|} \cdot \mathbf{e}_j \right|, & \text{otherwise} \end{cases} \quad (5)$$

In Eq. (5), \mathbf{e}_j is the local orientation vector of vertex j estimated from the eigenvector whose eigenvalue is the maximum of the matrix $\mathbf{M}(\mathbf{v}_j)$. $\mathbf{M}(\mathbf{v}_j)$ is the 3×3 covariance matrix of difference position vectors between \mathbf{v}_j and its neighbors, $\{(\mathbf{q}_k - \mathbf{v}_j) \mid \mathbf{q}_k \in N(\mathbf{v}_j)\}$, where $N(\mathbf{v}_j) \subset V$ is the set of its k -nearest neighbors of \mathbf{v}_j . We set $k = 26$ in this study.

Because we extract vessel points explicitly and use non-contrast images, the distribution of the position vectors gives a

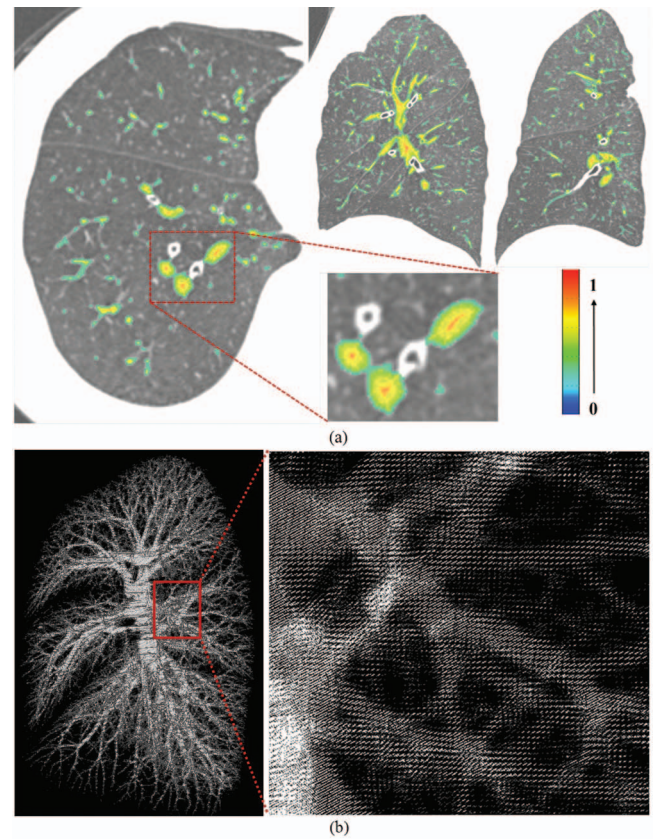


FIG. 7. Vertex weight computation result. (a) Sectional view of the total vertex weight. (b) 3D points rendering with weights as grey-scale intensity.

better result than the distribution of intensities estimated from the Hessian of I . Figure 8 shows a comparison between the two approaches. We compute \mathbf{e}_j only for the boundary vertices whose distance $\Phi(\mathbf{v}_j) < 2\sqrt{d_x^2 + d_y^2 + d_z^2}$ and set this to $\mathbf{0}$ otherwise, as the orientation of the spherelike point is difficult to estimate with this approach.

In summary, from a given vertex, the construction energy is minimized when connecting to a spatially close vertex with a greater weight as an edge whose direction is similar to that of the vascular flow. Conversely, the probability that it is classified in the same group is low with the vertex far away or in a different direction from the proceeding direction of the vessel. Equation (3) shows the result reflected by given these three considerations.

IV.A.3. Computation

To solve this problem precisely, we should start from the directed graph connected by all of the combinations of vertices. For computational efficiency, we compute a Delaunay triangulation first to reduce the number of neighbors of each vertex, after which we explore a subgraph among possible combinations using the Dijkstra algorithm. To obtain a meaningful result, we use a weighted Delaunay triangulation known as regular triangulation using the CGAL library.³⁸

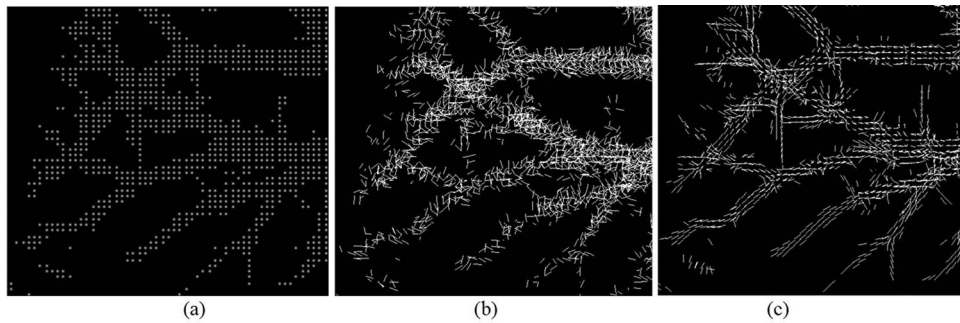


FIG. 8. Comparison of orientation estimation. (a) Original point set in 3D. (b) Local orientations using a Hessian of I . (c) Local orientations using a covariance matrix of positional differences.

After computing the weighted Delaunay triangulation only using vertex weights, we apply the Dijkstra algorithm reflecting the edge cost in Eq. (3) from one or several seed points. Seed points may be obtained by means of user interaction or can be selected from the local maxima of the vertex weights in the mediastinal region. Theoretically, the result of the minimum spanning tree is only affected by edge costs. In our case, the edge cost between two vertices can be differed from parent-child relationship in Eq. (5). However, we set the vertex with higher vertex weight as a parent and the other vertex as a child. Therefore, their relationship is not changed by seed point, but only decided by their relative weights. Therefore, seed points are independent on the results, but only required to proceed with the algorithm. They can be decided manually or automatically, and composed of a single or multiple points. However, for the full automatic processing, we set local maxima of vertex weights as initial seed points in our implementation.

In the case of the Euclidean MST (EMST), it is well known that EMST is a complete subgraph of the Delaunay triangulation.³⁹ Although we cannot guarantee that our weighted EMST is a subgraph of the weighted Delaunay triangulation due to the edge weights, it works well in practice. Limitations are discussed in Sec. VII.

Figure 9 shows the initial tree from the point set by weighted Delaunay triangulation and the MST. Given that the MST is a global structure, it provides a good solution for explicitly separated point sets when only Euclidean distances are used as weights. However, because there is no preference for the same distances, there is no guarantee that we will not connect the edges of the crossing cases shown in Fig. 1. As shown in Fig. 10(a) the connection direction between points is determined by the priority of the search direction. However, our modified MST is constructed in a manner similar to the diffusion from the vascular center toward the wall, as shown in Figs. 10(b) and 10(c).

IV.B. Refinement

After constructing a MST T for V , we refine the point clouds as a refined tree structure. This step stems from Livny's original work,²⁷ except that the weight w computed in the previous step is used. In that study,²⁷ an orientation vector

field \mathbf{o} is generated to refine the tree structure by solving the global optimization problem delineated in Eq. (6). This equation makes the orientation vectors similar to the edge direction and maintains a similar direction between a vertex \mathbf{v}_i and its

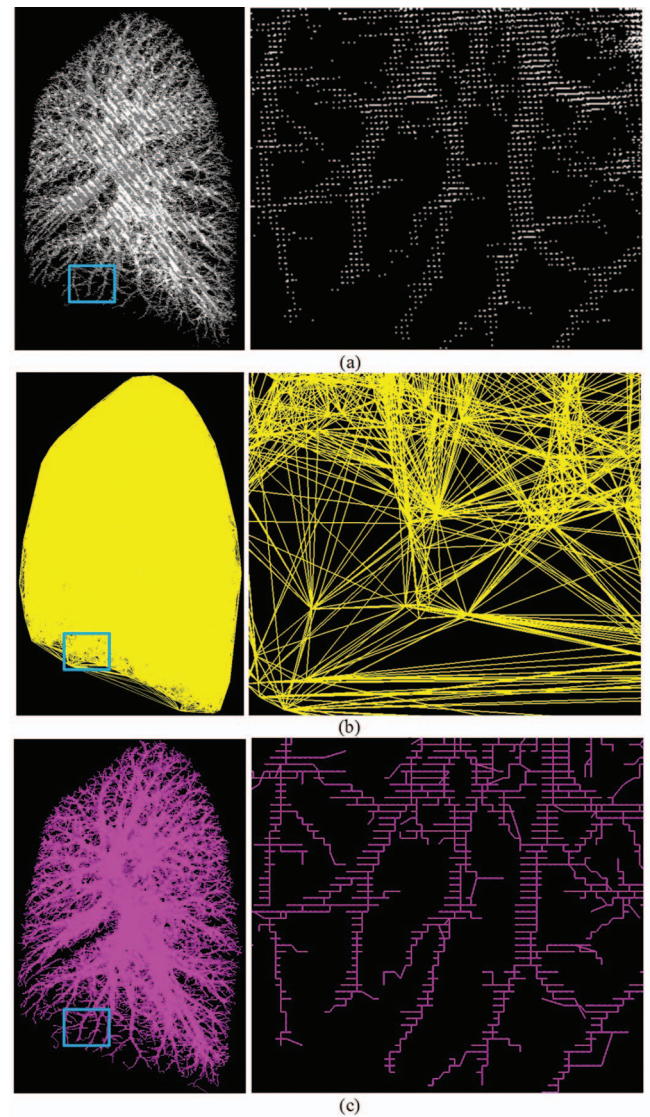


FIG. 9. Tree construction steps. (a) Initial point set extraciton. (b) weighted Delaunay triangulation. (c) MST.

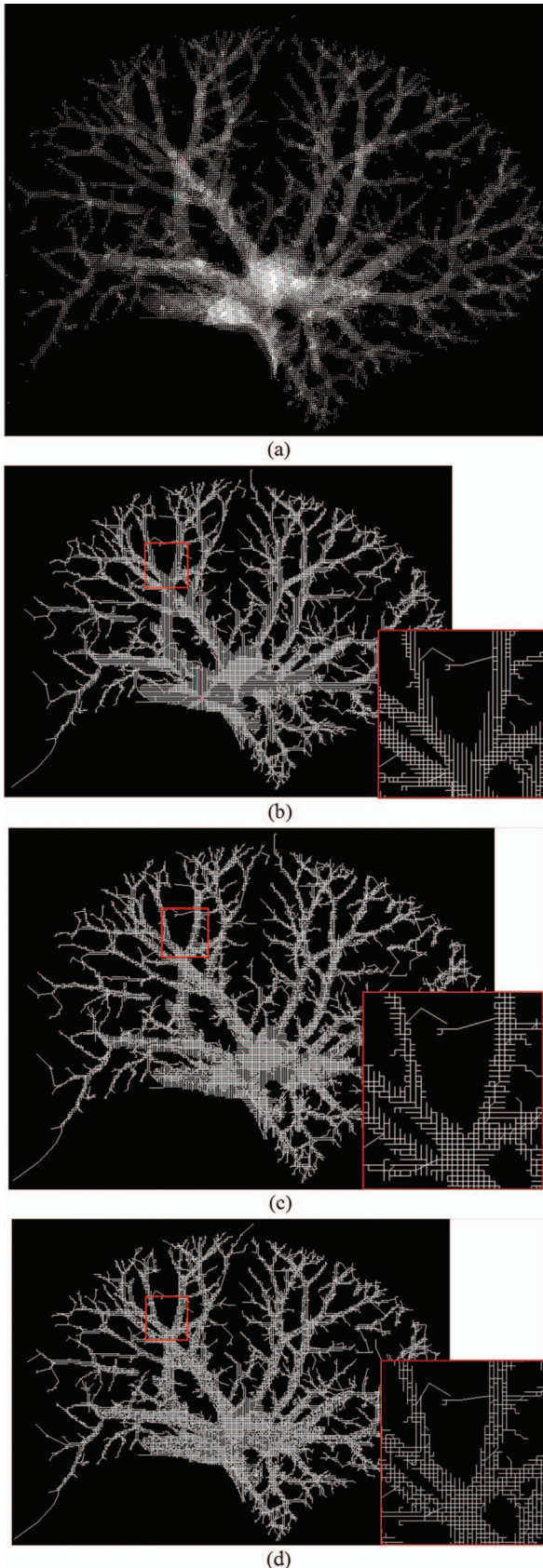


FIG. 10. EMST vs weighted EMST; vascular points are extracted from only 30 consecutive slices in total 528 chest CT slices. All the images are rotated 90° in the clockwise direction from the axial view direction. (a) Original point set (in 3D). (b) EMST. (c) MST using vertex weights. (d) MST using vertex weights and edge weights.

parent \mathbf{v}_i^p . Each $\Delta E(T)$ and $\Delta O(T)$ term is matched.

$$\min_{\mathbf{o}} \{\Delta E(T) + \Delta O(T)\}$$

$$\begin{aligned} \Delta E(T) &= \sum_{\mathbf{v}_i \in V} \left(w_i \left\| \mathbf{o}_i - \frac{(\mathbf{v}_i^p - \mathbf{v}_i)}{\|\mathbf{v}_i^p - \mathbf{v}_i\|} \right\|^2 \right)^2, \\ \Delta O(T) &= \sum_{\mathbf{v}_i \in V} \left(\frac{w_i^p + w_i}{2} \left\| \mathbf{o}_i^p + \mathbf{o}_i \right\|^2 \right)^2. \end{aligned} \quad (6)$$

Although local orientation vectors $\{\mathbf{e}_i\}$ are estimated in the previous step, we compute orientation vectors by global optimization again because we cannot obtain \mathbf{e} for vertices which are not on the boundary. $\{\mathbf{o}_i\}$ is used for the re-grouping in Sec. V.B as well as for the refinement process in this step. The initial tree is refined by solving Eq. (7). This equation minimizes the sum of the error terms $\Delta A(T)$ to make the edges smooth and $\Delta F(T)$ to maintain the initial tree geometry.

$$\min_{\mathbf{v}} \{\Delta A(T) + \Delta F(T)\}$$

$$\begin{aligned} \Delta A(T_i) &= \sum_{e(\mathbf{u}, \mathbf{v}) \in T} \left(\frac{w_u + w_v}{2} \left\| (\mathbf{u}' - \mathbf{v}') - \frac{\|\mathbf{u} - \mathbf{v}\|(\mathbf{o}_u + \mathbf{o}_v)}{\|\mathbf{o}_u + \mathbf{o}_v\|} \right\|^2 \right), \\ \Delta F(T) &= \sum_{e(\mathbf{u}, \mathbf{v}) \in T} \left(w_v \left\| \frac{\mathbf{u}' + \mathbf{v}'}{2} - \frac{\mathbf{u} + \mathbf{v}}{2} \right\|^2 \right). \end{aligned} \quad (7)$$

Here, \mathbf{u}', \mathbf{v}' denotes the refined position of the original vertex position \mathbf{u}, \mathbf{v} of an edge $e(\mathbf{u}, \mathbf{v})$.

Figure 11 shows the refined tree from the initial MST. More details can be found in the original work.²⁷ The solutions to Eqs. (6) and (7) can be obtained easily by conversion to the linear equations. Note that we do not move the initial vertices, but only save refined positions additionally, as the initial positions of the vertices are the accurate vessel points and because the refined tree is required to obtain a simple skeletal structure when dividing different branches in the subsequent step. Therefore, we store the refined tree T' and vertex correspondences to T .

V. CLASSIFICATION OF VESSELS

V.A. Separation of branches

It is difficult to separate arteries and veins in the mediastinal region of the lung because they are nearly attached. Therefore, we separate them by cutting off vascular branches beyond a certain branching level. To do this, we assign labels D to each edge of T' . From the leaf nodes to the center, the label value increases according to the rules shown in Eq. (8).

$$D(e) = \begin{cases} 1, & \text{if } e \text{ contains a leaf node} \\ \max\{D(e_C)\} + 1, & \text{otherwise} \end{cases} \quad (8)$$

Here, e_C denotes the children edges of e . Figure 12 shows a gray-scaled tree according to the label value of each edge. The

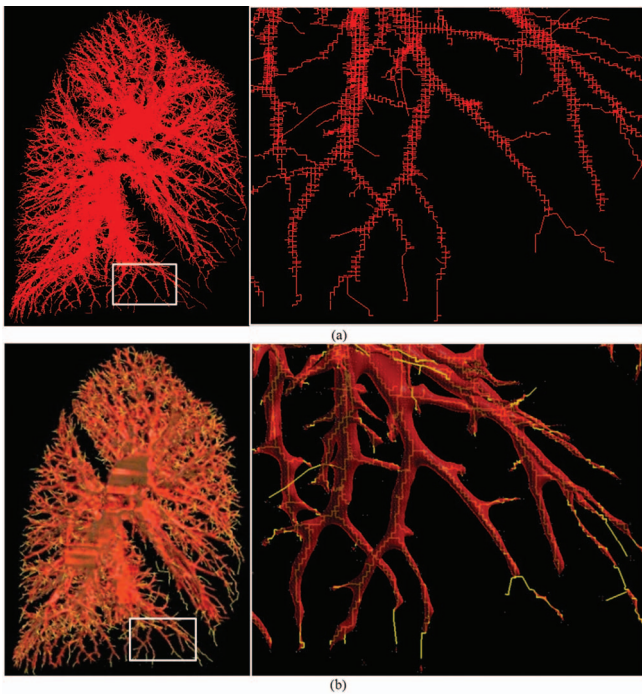


FIG. 11. Tree refinement; the figures on the right in (a) and (b) show zoomed-in views of the white regions in the corresponding figures on the left; the refined tree in (b) is displayed with the red vascular surfaces to check the skeletal structure. (a) Initial tree. (b) Refined tree (center lines) with surface rendering.

tree is dark gray at a lower label and becomes brighter as the values increase.

After assigning depth levels from the periphery, the next step is to cut off the edges and their children whose labels are larger than a user-defined constant value. A tree T can then be split into several connected substructures, as shown in Fig. 13. In this step, the automated result may not be satisfactory, but it can be easily revised by user interaction when a user selects the volume of interest (VOI) using 3D balls or boxes.

V.B. Regrouping

One of our contributions is that the separation and the union can be handled in the same framework of vascular tree

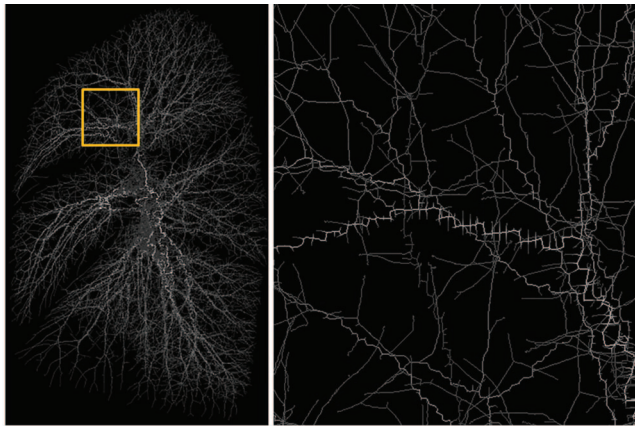


FIG. 12. Edge labeling. Right figure – enlarged region of the orange box on the left.

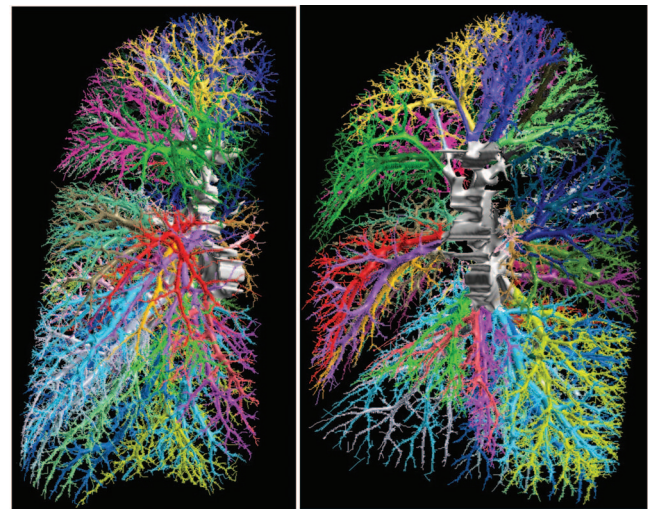


FIG. 13. Vascular subbranches of a right lung; coronal view (left) and sagittal view (right); random coloring; each color represents one vascular branch and the white mediastinal region is the cropped area.

construction. For the cut region in the previous step, we extract only vertices and reconstruct edges from each root of a branch, the leaf node connected to the edge with the highest label value in the same branch, via the same method used in Sec. IV.A. N seed points are selected from N branches for the propagation algorithm. One different element is that the orientation vector \mathbf{e}_i is replaced by \mathbf{o}_i when computing e_{ij} in Eq. (5), as points in the distal region are mostly classified to the sphere-like shapes, making it difficult to estimate their orientations. In addition, the vertices propagating from different seed points are classified as belonging to different groups. Figure 14 show the reconstruction results from the clipped branches.

For the branches whose trunks meet, we merge them into one group. A vascular branch can be considered as a set of cylindrical segments whose centers are the longest connected edges and whose radii are obtained from Φ , the distance field introduced in Sec. IV.A.1. We expand the i th branch from its root position \mathbf{r}_i to the orientation direction of \mathbf{r}_i with a cylinder whose radius, $R_i = \max\{\Phi(\mathbf{v}_j) \mid \mathbf{v}_j \text{ is any vertex included in branch } i\}$. If it intersects with the nearest branch from \mathbf{r}_i and the maximum sectional area of this intersection exceeds 50%

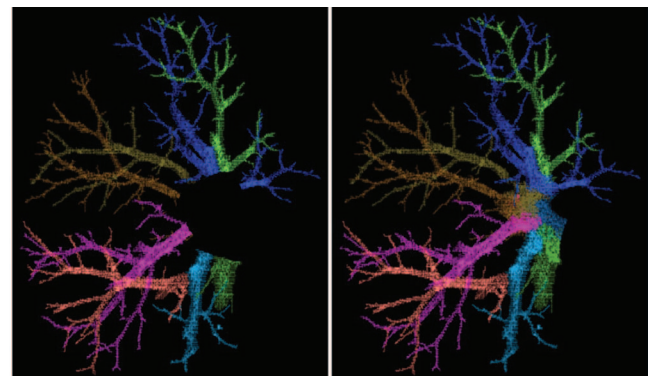


FIG. 14. Diffusion to the proximal entry.

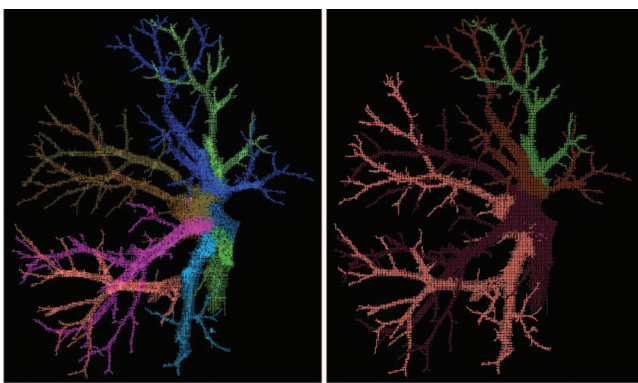


FIG. 15. Union of branches; from eight groups to four groups using our remerging scheme.

of πR_i^2 , we merge two branches. The threshold value, 50%, may be changed, but we apply conservative merging criteria in the automated algorithm since this step may not be successful for all cases. We start from the narrowest vessel, and run this scheme iteratively until there are no possible candidates.

Figure 15 shows the union result of the example in Fig. 14. After reducing the number of groups as much as possible, the remaining branches can be combined easily through user interaction.

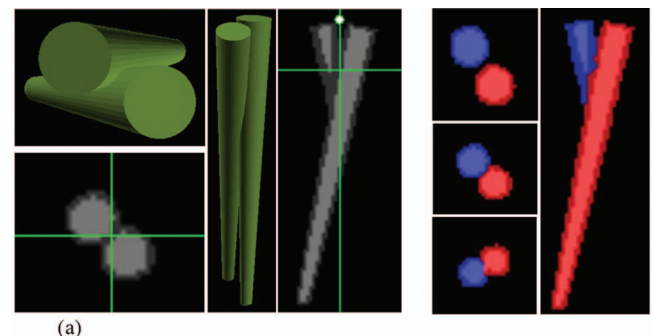
VI. EXPERIMENTAL RESULTS

Because it is nearly impossible to evaluate the proposed approach accurately with real live lungs, we approach the evaluation in two ways: using a mathematical virtual phantom and obtaining visual scores from human experts.

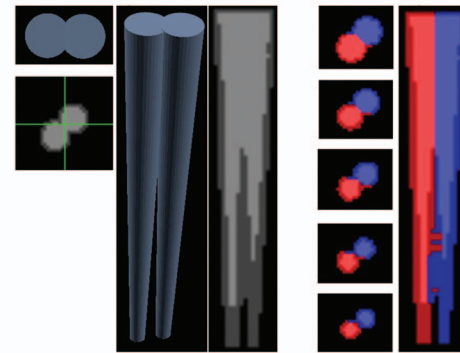
For technical validation of the crossing and parallel cases of classification as attempted in earlier work in Ref. 24, we devised a virtual mathematical phantom and evaluated the cases shown in Fig. 16. In addition, Fig. 17 shows the results of similar cases with real patient CT data. The accuracy of the result for these phantom data is computed as the ratio of the number of correctly classified voxels to the whole number of vascular voxels in the virtual CT. The type of an overlapped cell by two different vessels is considered as the type of vessel occupying more volumes. The evaluation results are 99.6% for the example shown in Fig. 16(a) and 99.1% for Fig. 16(b).

For clinical validation, ten noncontrast volumetric chest CT scans at full inspiration of patients with chronic obstructive pulmonary disease (COPD) with submillimeter thicknesses were used. Among preobtained chest CT scans of COPD patients for the research purpose at the Asan Medical Center, the ten smallest emphysema index valued set without nodules were selected in order to use the data close to normal. Our algorithm does not depend on the respiratory phase, but we use full-inspiration images for a consistent comparison.

One of the authors (S. M. Lee), a thoracic radiologist with eight years of experience assessed the accuracy of automated classification results of ten segments of the right lung using a grading system on a scale of 0–10, where the scores represent the fidelity of the classification results from 0:0% to 10:100%. The evaluation process was done in the following way. Using



(a)



(b)

FIG. 16. Mathematical phantom generation and classification result; the volume and classification results are represented as virtual CT images by generating sectional images. (a) A crossing vessels; 3D model and volume (left); result (right). (b) An adjacent case in parallel.

our developed software, user can select one of the branches, represented as one color. The selected branch is mapped to the CT image with its color. The evaluator checks all the slices spanned by the selected branch. If the branch is mapped to one type of vessel, then he assigns ten score to the branch. Otherwise, the score was given as the tenfold of the ratio of the number of slices occupied by incorrectly classified vessels to the total count of slices spanned by the branch. He repeated this process until all of the branches are determined their type, and then checked branches again in the same way after color mapping as shown in the right figure of Fig. 17(a). Finally, the round-off average value was computed for each segment.

Because it is hard to argue that this visual scoring is ‘real’ quantification, we tried to quantify the accuracy of our algorithm in a different way. For two patients, incorrect branching positions were checked by a human expert, and the branch was separated to two children by removing the edge connected at that position. The volume portion of the smaller child branches to the total volume of the vessels was computed as the error rate. The score value for each segment is represented in Table I. The left column of each segment represents the visual score, and the right column shows the quantified vascular volume portion (%) that was correctly classified.

As shown in Table I, our algorithm shows a classification capability level that exceeds 90%, despite the fact that there are several regions with low scores (RUL2 and RUL3 for patient 6). However, the scores only represent the classification results without considering the accuracy of initial vessel

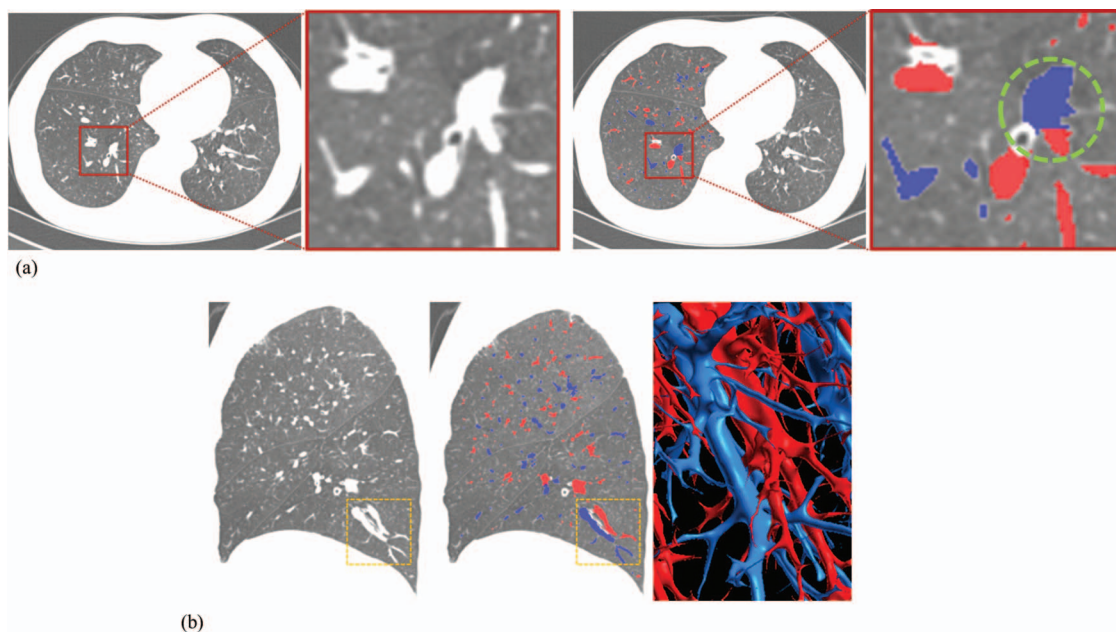


FIG. 17. Difficult cases and classification results. (a) A crossing case; original CT (left) and the classification result (right); the right box of each image is enlarged region of the box on the left image; the region in the dashed circle shows separation of attached vessels in the CT image. (b) An adjacent case in parallel; the original CT image in the sagittal view (left), the classification result in the same view (middle), and the 3D rendering of the classification result in the dashed box of the left images.

segmentation. Thus it is necessary to expand the number of cases and to test each step for a more accurate and meaningful evaluation in future studies.

VII. DISCUSSION AND CONCLUSION

In this paper, we suggest an algorithm for the automated separation of the pulmonary vessels from CT images which involves constructing a tree by minimizing the construction energy. Different vascular branches are separated by cutting the mediastinal region and are then remerged by propagating the clipped region from each branch (Fig. 18). Our method is applicable to noncontrast and contrast CT images because it

filters nonvascular structures and introduces weights to make the tree construction process insensitive to noise. By constructing explicit tree structures for all of the voxels representing vessels, our resulting structure is very effective for various postprocessing works. Examples include geometrical property analyses (e.g., radius calculations) and substructure extractions (e.g., extracting subtrees under a certain distance or with a lower label value from the lung periphery).

In contrast to the original tree reconstruction approach from unorganized point sets, we assign meaningful weights to the vertices for accuracy and construct a tree by optimization. This approach imparts greater fidelity to the original vessel structures. We also classify different types of vessels

TABLE I. Visual scoring and accuracy estimation for classification.

Patient no.	Region ^a															Average						
	RUL1		RUL2		RUL3		RML1		RML2		RLL1		RLL2		RLL3		RLL4					
1	10	100	10	100	10	100	10	100	10	100	10	100	10	100	9	92	8	90	10	100	9.7	98
2	9	94	9	92	8	87	6	75	9	89	10	100	7	81	10	100	10	100	10	100	8.8	91
3	10		9		10		7		8		10		8		10		10		10		9.2	
4	6		9		10		8		10		9		10		10		9		9		9.0	
5	10		8		10		8		10		10		10		10		8		9		9.3	
6	8		7		7		8		8		9		10		9		10		10		8.6	
7	9		10		10		8		7		10		10		10		9		10		9.3	
8	10		10		10		8		10		9		10		10		9		10		9.6	
9	9		10		10		8		10		10		8		8		9		7		8.9	
10	9		9		10		9		10		10		10		10		9		8		9.4	
Total mean																	9.18					

^aRUL1 – right superior lobe apical segment, RUL2 – posterior segment, RUL3 – anterior segment, RML1 – right middle lobe lateral segment, RML2 – medial segment, RLL1 – right interior lobe superior segment, RLL2 – medial basal segment, RLL3 – anterior basal segment, RLL4 – lateral basal segment, and RLL10 – posterior basal segment.

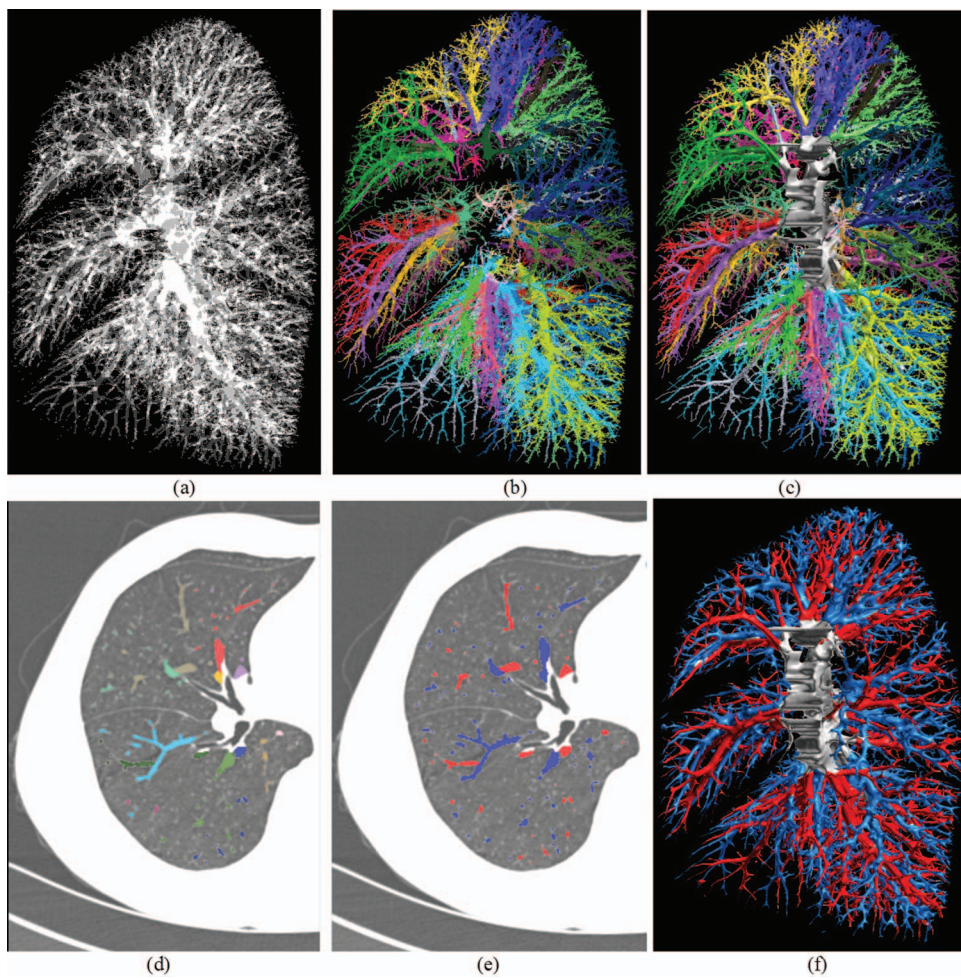


FIG. 18. 3D examples; (a) initial point set, (b) vessel branch segmentation, (c) surface fitting and rendering of each group, (d) remapping to the CT images, (e) merged vessels to arteries and veins, and (f) surface fitting and rendering of the finally classified vessels.

automatically by constructing a MST and cutting out the root part using automatically assigned labels.

Our results show satisfactory levels of accuracy acceptances in experiments as well as in a medical evaluation. The classification accuracy is affected by the quality of the initial vessel extraction; the vessel points are over-extracted and the nonvessel points act as noise. This may be caused by the fixed attenuation reference value when extracting vessels, despite the diversity of patients as well as variants due to disease. For further study, a more robust initial vessel extraction process can be evaluated. Related to validation method, it is required to evaluate data using the quantitative way. The sensitivity analysis of parameters and optimization then can be performed with quantitative analysis of the accuracy. In addition, the experiments for various data types, such as the data of patient with various diseases, are also necessary to check the applicability of our algorithm. The improvement of computational efficiency is also one of the remaining works for usability. In our experiment, it takes about 30~40 min for the whole automatic process depending on the number of vascular points. The most time-consuming step in our implementation is the MST construction part. This step can be improved by

design of efficient data structure, hierarchical computing, or parallel processing.

As noted in Sec. IV.B.3, the construction algorithm of the MST does not guarantee that the MST result is the solution to Eq. (1) because we limit possible edge connections by means of weighted Delaunay triangulation, which considers only vertex weights. This gives desirable solutions, as most of points are distributed evenly except for those on the periphery, and because the portion of e_{ij} is only 1/5 in our setting. e_{ij} works only when two small vessels are crossing and when it is necessary to determine their origins.

This fully or semiautomatic classification approach may be useful when assessing many pulmonary diseases, such as pulmonary hypertension, interstitial lung disease and COPD. For clinical use, however, it is necessary to find failure patterns and to introduce patient-specific parameters.

ACKNOWLEDGMENT

This work was supported by the Technology Innovation Program (10041618) funded by the Ministry of Knowledge Economy (MKE) of Korea.

- ^aAuthor to whom correspondence should be addressed. Electronic mail: namkugkim@gmail.com; Telephone: +82-2-3010-6573
- ¹A. J. Buckler, L. Bresolin, N. R. Dunnick, and D. C. Sullivan, and for the Group, "A collaborative enterprise for multi-stakeholder participation in the advancement of quantitative imaging," *Radiology* **258**(3), 906–914 (2011).
- ²S. Santos, V. I. Peinado, J. Ramirez, J. Morales-Blanbir, R. Bastos, J. Roca, R. Rodriguez-Roisin, and J. A. Barbera, "Enhanced expression of vascular endothelial growth factor in pulmonary arteries of smokers and patients with moderate chronic obstructive pulmonary disease," *Am. J. Respir. Crit. Care Med.* **167**, 1250–1256 (2003).
- ³Y. Kasahara, R. M. Tudor, C. D. Cool, D. A. Lynch, S. C. Flores, and N. F. Voelkel, "Endothelial cell death and decreased expression of vascular endothelial growth factor and vascular endothelial growth factor receptor 2 in emphysema," *Am. J. Respir. Crit. Care Med.* **163**, 737–744 (2001).
- ⁴N. F. Voelkel, R. W. Vandivier, and R. M. Tudor, "Vascular endothelial growth factor in the lung," *Am. J. Physiol. Lung Cell. Mol. Physiol.* **290**, L209–L221 (2006).
- ⁵S. Matsuoka, G. R. Washko, M. T. Dransfield, T. Yamashiro, R. S. Jose Estepar, A. Diaz, E. K. Silverman, S. Patz, and H. Hatabu, "Quantitative CT measurement of cross-sectional area of small pulmonary vessel in COPD: Correlations with emphysema and airflow limitation," *Acad. Radiol.* **17**, 93–99 (2010).
- ⁶I. Uejima, S. Matsuoka, T. Yamashiro, K. Yagihashi, Y. Kurihara, and Y. Nakajima, "Quantitative computed tomographic measurement of a cross-sectional area of a small pulmonary vessel in nonsmokers without airflow limitation," *Jpn. J. Radiol.* **29**, 251–255 (2011).
- ⁷A. Bejan and S. Lorente, "The constructal law of design and evolution in nature," *Philos. Trans. R. Soc. London, Ser. B* **365**, 1335–1347 (2010).
- ⁸C. Lorenz, I.-C. Carlsen, T. M. Buzug, C. Fassnacht, and J. Weese, "A multi-scale line filter with automatic scale selection based on the Hessian matrix for medical image segmentation," *Scale-Space Theories in Computer Vision, Lecture Notes in Computer Sciences Vol. 1252* (Springer, Berlin, 1997), pp. 152–163.
- ⁹Y. Sato, S. Nakajima, N. Shiraga, H. Atsumi, S. Yoshida, T. Koller, G. Gerig, and R. Kikinis, "Three-dimensional multi-scale line filter for segmentation and visualization of curvilinear structures in medical images," *Med. Image Anal.* **2**(2), 143–168 (1998).
- ¹⁰T. McInerney and D. Terzopoulos, "T-snakes: Topology adaptive snakes," *Med. Image Anal.* **4**(2), 73–91 (2000).
- ¹¹L. M. Lorigo, O. D. Faugeras, W. E. L. Grimson, R. Keriven, R. Kikinis, A. Nabavi, and C.-F. Westin, "CURVES: Curve evolution for vessel segmentation," *Med. Image Anal.* **5**, 195–206 (2001).
- ¹²T. Bülow, C. Lorenz, and S. Renisch, "A general framework for tree segmentation and reconstruction from medical volume data," *Medical Image Computing and Computer-Assisted Intervention – MICCAI 2004, Lecture Notes in Computer Science Vol. 3216* (Springer, Berlin, 2004), pp. 533–540.
- ¹³S. Bouix, K. Siddiqi, and A. Tannenbaum, "Flux driven automatic centerline extraction," *Med. Image Anal.* **9**, 209–221 (2005).
- ¹⁴S. Hu, E. A. Hoffman, and J. M. Reinhardt, "Automatic lung segmentation for accurate quantitation of volumetric X-ray CT images," *IEEE Trans. Med. Imaging* **20**(6), 490–498 (2001).
- ¹⁵C. Zhou, H.-P. Chan, L. M. Hadjiiski, S. Patel, P. N. Cascade, B. Sahiner, J. Wei, J. Ge, and E. A. Kazerooni, "Automatic pulmonary vessel segmentation in 3D computed tomographic pulmonary angiographic (CTPA) images," *Proc. SPIE* **6144**, 1524–1530 (2006).
- ¹⁶C. Zhou, H.-P. Chan, B. Sahiner, L. M. Hadjiiski, A. Chunghai, S. Patel, J. Wei, J. Ge, P. N. Cascade, and E. A. Kazerooni, "Automatic multiscale enhancement and segmentation of pulmonary vessels in CT pulmonary angiography images for CAD applications," *Med. Phys.* **34**(12), 4567–4577 (2007).
- ¹⁷H. Zhang, Z. Bian, D. Jiang, Z. Yuan, and M. Ye, "Level set method for pulmonary vessels extraction," in *Proceedings of IEEE International Conference on Image Processing* Barcelona, Spain (IEEE, 2003), pp. 1105–1108, 2003.
- ¹⁸X. Zhu, Z. Xue, X. Gao, Y. Zhu, and S. T. C. Wong, "VOLES: Vascularity-Oriented LEvel Set algorithm for pulmonary vessel segmentation in image guided intervention therapy," in *Proceedings of IEEE International Symposium on Biomedical Imaging (ISBI)* Boston, MA, 2009 (IEEE, NJ, 2009), pp. 1247–1250.
- ¹⁹J. N. Kaftan, A. P. Kiraly, A. Bakai, M. Das, C. L. Novak, and T. Aach, "Fuzzy pulmonary vessel segmentation in contrast enhanced CT data," *Proc. SPIE* **6914**, 69141Q1–69141Q12 (2008).
- ²⁰G. Agam, S. G. Armato III, and C. Wu, "Vessel tree reconstruction in thoracic CT scans with application to nodule detection," *IEEE Trans. Med. Imaging* **24**(4), 486–499 (2005).
- ²¹T. Tozaki, Y. Kawata, N. Niki, and H. Ohmatsu, "Extraction and classification of pulmonary organs based on thoracic 3D CT images," *Syst. Comput. Jpn.* **32**(9), 42–53 (2001).
- ²²B. Chen, T. Kitasaka, H. Honma, H. Takabatake, M. Mori, H. Natori, and K. Mori, "Automatic segmentation of pulmonary blood vessels and nodules based on local intensity structure analysis and surface propagation in 3D chest CT images," *Int. J. Comput. Assist. Radiol. Surg.* **7**(3), 465–482 (2012).
- ²³T. Buelow, R. Wiemker, T. Blaffert, C. Lorenz, and S. Renisch, "Automatic extraction of the pulmonary artery tree from multi-slice CT data," *Proc. SPIE* **5746**, 730–740 (2005).
- ²⁴P. K. Saha, Z. Gao, S. K. Alford, M. Sonka, and E. A. Hoffman, "Topomorphic separation of fused isointensity objects via multiscale opening: Separating arteries and veins in 3D pulmonary CT," *IEEE Trans. Med. Imaging* **29**(3), 840–851 (2010).
- ²⁵R. Wiemker, T. Bülow, and R. Opfer, "Automated hierarchical partitioning of anatomical trees," *Proc. SPIE* **6511**, 65110G1–65110G9 (2007).
- ²⁶Z. Gao, R. W. Grout, C. Holtze, E. A. Hoffman, and P. K. Saha, "A new paradigm of interactive artery/vein separation in noncontrast pulmonary CT imaging using multiscale topomorphic opening," *IEEE Trans. Biomed. Eng.* **59**(11), 3016–3027 (2012).
- ²⁷Y. Livny, F. Yan, M. Olson, B. Chen, H. Zhang, and J. El-Sana, "Automatic reconstruction of tree skeletal structures from point clouds," *ACM Trans. Graphics* **29**(6), 1–8 (2010).
- ²⁸P. Tan, G. Zeng, J. Wang, S. B. Kang, and L. Quan, "Image-based tree modeling," *ACM Trans. Graphics* **26**(3), 1–8 (2007).
- ²⁹A. Tagliasacchi, H. Zhang, and D. Cohen-Or, "Curve skeleton extraction from incomplete point cloud," *ACM Trans. Graphics* **28**(4), 1–10 (2009).
- ³⁰G. Li, L. Liu, H. Zheng, and N. J. Mitra, "Analysis, reconstruction and manipulation using arterial snakes," *ACM Trans. Graphics* **29**(6), 1–10 (2010).
- ³¹M. S. Hassouna and A. A. Farag, "Variational curve skeletons using gradient vector flow," *IEEE Trans. Pattern Anal. Mach. Intell.* **31**(12), 2257–2274 (2009).
- ³²VESSEL 2012 [Online], see <http://vessel12.grand-challenge.org/>, 2012.
- ³³H. Shikata, G. McLennan, E. A. Hoffman, and M. Sonka, "Segmentation of pulmonary vascular trees from thoracic 3D CT images," *Int. J. Biomed. Imaging* **2009**, 1–11 (2009).
- ³⁴R. Pohle and K. D. Toennies, "Segmentation of medical images using adaptive region growing," *Proc. SPIE* **4322**, 1337–1346 (2001).
- ³⁵T. Koller, G. Gerig, G. Szekely, and D. Dettwiler, "Multiscale detection of curvilinear structures in 2D and 3D image data," in *Proceedings of IEEE International Conference on Computer Vision*, Washington, DC (IEEE Computer Society, Washington, 1995), pp. 864–869.
- ³⁶D. Lesage, E. D. Angelini, I. Bloch, and G. Funka-Lea, "A review of 3D vessel lumen segmentation techniques: Models, features, and extraction schemes," *Med. Image Anal.* **13**, 819–845 (2009).
- ³⁷S. Z. Zhao, X. Y. Xy, A. D. Hyghe, S. A. Thom, A. V. Stanton, B. Ariff, and Q. Long, "Blood flow and vessel mechanics in a physiologically realistic model of a human carotid arterial bifurcation," *J. Biomech.* **33**(8), 975–984 (2000).
- ³⁸See <http://www.cgal.org> for online CGAL library.
- ³⁹M. de Berg, M. van Kreveld, M. Overmars, and O. Schwarzkopf, *Computational Geometry: Algorithms and Applications (2/E)* (Springer, Berlin, 1997).